Single-crystal-like hematite colloidal nanocrystal clusters: synthesis and applications in gas sensors, photocatalysis and water treatment†

Xiao-Liang Fang, Cheng Chen, Ming-Shang Jin, Qin Kuang,* Zhao-Xiong Xie, Su-Yuan Xie,* Rong-Bin Huang and Lan-Sun Zheng

Received 12th March 2009, Accepted 4th June 2009
First published as an Advance Article on the web 6th July 2009
DOI: 10.1039/b905034e

A facile and efficient one-pot solvothermal synthetic route based on a simplified self-assembly is proposed to fabricate spherical hematite colloidal nanocrystal clusters (CNCs) of uniform shape and size. The as-prepared hematite CNCs are composed of numerous nanocrystals of approximately 20 nm in size, and present a single-crystal-like characteristic. A possible formation process based on the nucleation–oriented aggregation–recrystallization mechanism is proposed. Our experiments demonstrated that both the surfactant and the mixed solvent play very critical roles in controlling the size of primary nanocrystals and the final morphology of single-crystal-like spherical CNCs. Compared with other hematite nanostructures, the spherical hematite CNCs show outstanding performance in gas sensing, photocatalysis and water treatment due to their large surface area and porous structure. In addition, interesting tertiary CNCs formed by further assembly of secondary spherical CNCs were observed for the first time.

Introduction

Design and synthesis of the morphology-controlled colloidal nanocrystals have been intensively pursued in the past decade for their size and shape-dependent properties.[1–4] Recently, great success in high-quality nanocrystal synthesis has enabled chemists to devote more efforts to the exploration of secondary assemblies with precisely controlled alignment due to their attractive applications in high performance electronic, optical, or magnetic nanodevices.[5–8] By using monodisperse colloidal nanocrystals as building blocks, various 1D, 2D and 3D secondary assemblies (even super crystals of binary nanocrystal superlattice) have been successfully fabricated to date.[6–10] Among various synthetic methods, the most efficient strategy to fabricate 3D secondary assemblies is self-assembly,[11] in which colloidal nanocrystals spontaneously aggregate to form secondary assemblies under the cohesion effect of the "mortar", such as the surfactants, multifunctional organic ligands, polymers, or biomolecules.[12–18] However, most of the reported studies based on self-assembly are usually a multistep process that requires prefabricating colloidal nanocrystals before the self-assembly.[12–15] In practical application, it is more desirable to have a simplified self-assembly approach wherein spontaneous aggregation occurs with the formation of primary nanocrystals during a synthetic process. Nevertheless, successful syntheses based on a one-step self-assembling strategy are still rarely reported because of the lack of appropriate and generalized synthetic methodologies.[8a,16–18] From the viewpoint of fundamental research, it is still desirable to develop simple and efficient synthetic methodologies for secondary structured assemblies with designed chemical components and controlled morphologies.

α-Fe_2O_3 (hematite), as an n-type semiconductor ($E_g = 2.1$ eV), is the most stable iron oxide under ambient conditions. It has been intensively investigated due to its environmental safety and potential applications in gas sensors,[19–21] rechargeable lithium ion batteries,[19b,22] catalyst supports,[23] photodegradation,[24–26] waste-water treatment,[26–28] and biological and medical fields.[29] Over the past few years, various well-defined simple shapes of hematite nanostructures, such as rods, wires, belts, tubes, cubes, ellipsoids, rings, and spindles,[27–35] have been obtained successfully by a series of vapor-phase processes and solution-based routes, especially the solvent-assisted methods. Recently, hierarchical hematite nanostructures have attracted increasing attention.[26,36–38] In comparison with those simple nanostructures, hierarchical hematite nanostructures, such as hollow spheres assembled by nanosheets,[26] present more outstanding properties in gas sensing, photocatalysis and water treatment. However, the chemists found that hematite seems to be a material that shows a particular tendency toward mesocrystal formation. Simple[34,35] or hierarchical[37,38] hematite nanostructures are often composed of smaller subunits (*i.e.*, uniform crystallites of only a few nanometres in size) by oriented attachment so that they look like a single crystal. Although some possible mechanisms have been proposed,[39] there are still many factors influencing the formation of such special single-crystal-like hematite that are not yet understood. Moreover, it would be very useful to investigate their properties in facilitating a deeper understanding of morphology-controlled properties of hierarchical nanostructures.

State Key Laboratory for Physical Chemistry of Solid Surfaces and Department of Chemistry, College of Chemistry and Chemical Engineering, Xiamen University, Xiamen, 361005, P.R. China. E-mail: qkuang@xmu.edu.cn; syxie@xmu.edu.cn; Fax: +86 592 2183047; Tel: +86 592 2185191

† Electronic supplementary information (ESI) available: Schematic diagram of the gas sensing measurement system, SEM images of various spherical hematite CNCs synthesized under different solvent conditions and different amounts of PVP surfactant, and SEM image of commercial hematite powder. See DOI: 10.1039/b905034e

Herein, we report a facile one-step route to prepare single-crystal-like colloidal nanocrystal clusters (CNCs) of uniform spherical shape, each of which consists of oriented-attached hematite nanocrystals of approximately 20 nm in size. The effect of the surfactant PVP and mixed solvents tetrahydrofuran and ethanol was investigated to understand the formation mechanism of the hierarchical hematite CNCs. As far as we know, such single-crystal-like spherical hematite CNCs with uniform shape and size have not been reported heretofore, though similar CNCs of other species have been mentioned previously.[8a,16–18] In addition, for the first time, the prepared spherical hematite CNCs were further assembled as a kind of larger tertiary CNCs. Promising applications of these as-prepared spherical hematite CNCs in the surface-related fields including gas sensors, photocatalysis and water treatment were demonstrated.

Experimental

Synthesis of hematite CNCs

All the reagents were of analytical grade and used without further purification. Ferric chloride ($FeCl_3 \cdot 6H_2O$), urea, ethanol and tetrahydrofuran (THF) were purchased from Sinopharm Chemical Reagent Co. (Shanghai, China). The commercial hematite powder was purchased from Dachang Chemical Plant (Shanghai, China). Poly(*N*-vinyl-2-pyrrolidone) (PVP, MW = 40 000) was purchased from Alfa Aesar. In a typical experiment, $FeCl_3 \cdot 6H_2O$ (54 mg) and urea (24 mg) were added into the THF–ethanol mixture (16 mL, v/v of 1 : 1) and stirred until totally dissolved, followed by the addition of PVP (100 mg) under ultrasonic conditions for a few minutes. Then the suspension was transferred into a 20 mL Teflon-lined stainless steel autoclave. After sealing, the autoclave was warmed up at a rate of 1.5 °C min^{-1}, maintained at 180 °C for 12 h, and then cooled naturally. The product was collected by centrifugation, washed with deionized water and absolute ethanol several times, and finally dried in air at 60 °C for 6 h.

Characterization of the samples

The phase of the products was characterized by X-ray powder diffraction (XRD, Panalytical X'pert PRO diffractometer with Cu-Kα radiation). The morphologies and elemental compositions of the products were obtained by scanning electron microscopy (SEM, LEO 1530) equipped with energy-dispersive X-ray (EDX) spectroscopy. The structure of the products was obtained by high-resolution transmission electron microscopy (HRTEM, TECNAI F-30 with an accelerating voltage of 300 kV). The surface area of the final products was measured by the Brunauer–Emmett–Teller (BET) method using nitrogen adsorption and desorption isotherms on a Micrometrics ASAP 2020 system. Pore size distribution plot was obtained by the Barrett–Joyner–Halenda (BJH) method.

Gas sensing measurement

Gas sensing properties of the products were measured on a WS-30A gas sensing measurement system (Zhengzhou Winsen Electronics Technology Co., Ltd., PR China). The schematic diagram of the gas sensing measurement system is shown in Fig. S1 (see ESI†). The gas sensor was fabricated by coating an ethanol suspension of hematite sample onto a ceramic tube previously mounted with gold electrodes and platinum conducting wires. A resistor wire coil was crossed through the tube as a heater, which was able to provide the working temperature from 200–500 °C by adjusting the heating voltage. A reference resistance was put in series with the sensor to form a complete measurement circuit. In the test process, the voltage across the reference resistor changes with the sensor's resistance, which responds to the concentration of the detected gas. In our experiments, the gas sensors were sintered at 300 °C for 24 h to achieve stabilization before the measurement. Then an appropriate amount of ethanol as the detection target was injected into a closed test chamber and mixed with the air after complete thermal evaporation. The one-cycle test was completed when the sensor was exposed to air again by opening the chamber. Here, the responsivity of the sensor was defined as the ratio of the resistance in air (R_{air}) to that in ethanol gas (R_{gas}), *i.e.* R_{air}/R_{gas}. All the tests were operated under about 50% RH.

Photocatalysis measurement

Rhodamine B (RB) is used as a probe molecule to evaluate the photocatalytic properties of the as-synthesized hematite CNCs. In a typical experiment, a suspension of hematite photocatalysts (3 mL, 50 mg L^{-1}) was added to a quartz cell (1.0 cm × 1.0 cm × 4.5 cm). Then the RB solution (50 μL, 1.5 mmol L^{-1}) was injected into the quartz cell using a microinjector with continuous stirring under UV light irradiation from a 300 W high-pressure mercury lamp. The degree of RB degradation was monitored by the real-time detection of absorption at the wavelength of 553 nm using a Halogen Light Source HL-2000 system (Ocean Optics, Inc.). All the tests were carried out at room temperature.

Water treatment measurement

In a typical experiment, a chromium solution (20.80 mg L^{-1}) was prepared by using $K_2Cr_2O_7$ as the source of Cr^{VI}, and the pH value was adjusted to 3 by using HCl solution. Then, 20 mg of the adsorbent sample were added to 20 mL of the above solution under magnetic stirring at room temperature. After 24 h, the solid and liquid were separated by high-speed centrifugation (8000 rpm) for 8 min. The chromium concentration in the remaining solution was finally measured by atomic absorption spectrometry (Thermo Electron SOLAAR M6).

Results and discussion

Single-crystal-like spherical hematite CNCs were synthesized *via* a one-pot solvothermal reaction at 180 °C for 12 h, using $FeCl_3 \cdot 6H_2O$ and urea as the starting materials and THF–ethanol mixture as the solvent. PVP was employed as the surfactant to control the morphology of the product. After the reaction, a brick red precipitate was collected by centrifugation, and then washed with deionized water and absolute ethanol several times. The phase of the product was characterized by XRD. As shown in Fig. 1a, the XRD pattern of the product can be indexed to the rhombohedral phase of hematite (JCPDS no. 013-0534). Compared with the standard pattern, all the diffraction peaks are obviously widened but no preferential orientation is observed in

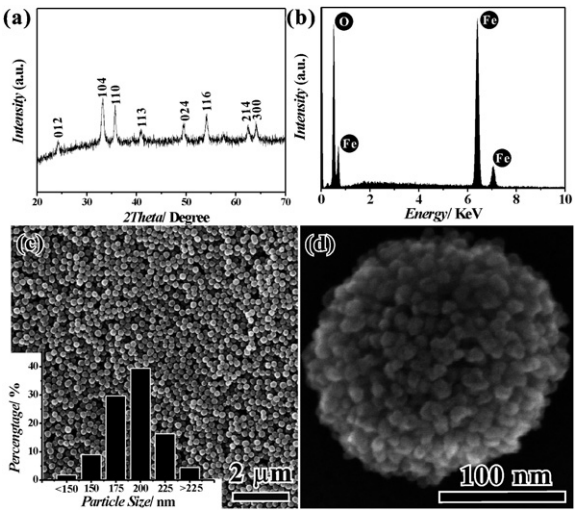

Fig. 1 Composition and morphology of the as-synthesized spherical hematite CNCs: (a) XRD pattern, (b) EDX spectrum, (c) low-magnification SEM image (inset: the histogram of size distribution), (d) typical high-magnification SEM image of an individual spherical hematite CNC.

the measured XRD pattern, suggesting the presence of very small hematite crystallites in the products. The average size of the hematite crystallites deduced from Sherrer's formula for the strongest peak (104) is about 20.6 nm. The elemental composition of the product was further confirmed by the EDX spectrum, which shows that the primary components are Fe and O (Fig. 1b). The morphology of the product was examined by SEM. Fig. 1c shows a typical low-magnification SEM image of the product, which indicates that the product is composed of a large quantity of well-dispersed spherical particles. These particles have uniform size and shape, most of which are 200 ± 25 nm in size estimated from SEM image (the inset of Fig. 1c). Meanwhile, the high-magnification SEM image (Fig. 1d) of an individual spherical particle reveals that these hematite particles are CNCs with a hierarchical architecture, and were built up from many single hematite crystallites of approximately 20 nm in size. The average crystallite size from the SEM image agrees well with the calculation result from the XRD pattern. Furthermore, some cavities with a diameter from 20 to 30 nm, which could be considered as stacking vacancies caused by the absence of subunits, are observed on the surface of hematite CNCs.

The internal structural information of the as-synthesized spherical hematite CNCs was obtained by TEM. As shown in Fig. 2a, many spots with a clear contrast difference in each individual spherical CNC were observed, suggesting that the CNCs consist of packed primary nanocrystals. A schematic model is inserted in Fig. 2a to illustrate the geometrical structure of hematite CNCs. The secondary structure of spherical CNCs can be observed more clearly in the high-magnification TEM image (Fig. 2b) of a typical isolated hematite CNC. Interestingly, the corresponding selected area electron diffraction (SAED) pattern (Fig. 2c), which was recorded from a whole particle of individual spherical hematite CNC (about 200 nm radiation diameter of electron beam was recorded), only presents a set of diffraction spots from the (001) zone axis. As the SAED pattern can reflect the internal crystal information of the whole particle, it can be concluded that the primary nanocrystals are highly

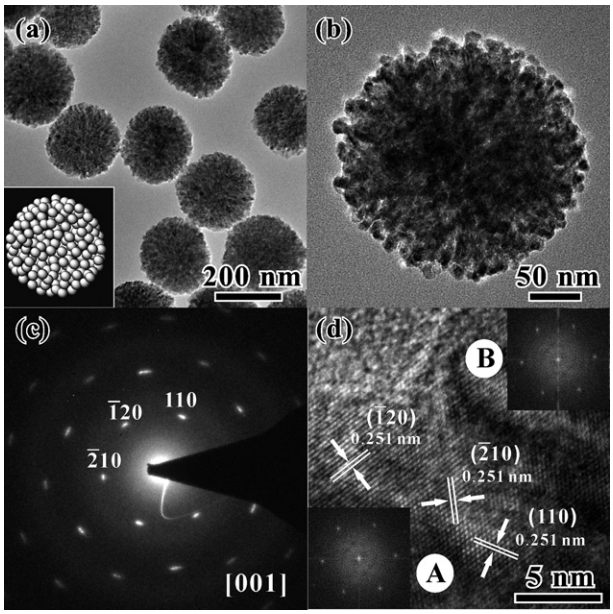

Fig. 2 TEM characterization of the as-synthesized spherical hematite CNCs: (a) low-magnification TEM image (inset: a schematic diagram that illustrates the microstructure of the aggregated hematite comprising packed nanocrystallites); (b) high-magnification TEM image and (c) the corresponding SAED pattern of an individual spherical hematite CNC, indicating the single-crystal-like nature of the CNCs; (d) HRTEM image taken from two adjacent primary nanocrystals marked with A and B (insets: the corresponding FFT patterns).

oriented within the CNCs so that the spherical CNCs have a single-crystal-like feature. Such single-crystal-like nature of the spherical CNCs is mirrored in an HRTEM image (Fig. 2d) taken from two adjacent primary nanocrystals. The two adjacent primary nanocrystals have almost the same crystallographic orientation, although a slight misalignment between the two primary nanocrystals can be observed (for example, approximately 1.3° mismatch between the (110) lattice fringes in the nanocrystals A and B). This misalignment accordingly accounts for the abnormal diffraction spots that are widened into narrow arcs.

Interestingly, when the initial concentration of Fe^{3+} was increased, a small quantity of tertiary CNCs, which formed by further spontaneous aggregation from spherical hematite CNCs, was observed in the product. As shown in Fig. 3a, the typical

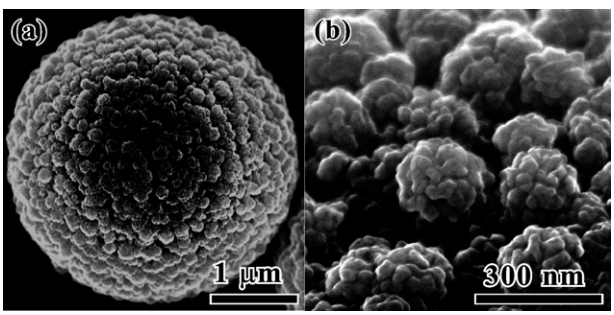

Fig. 3 Typical SEM images of an individual tertiary hematite aggregate: (a) low-magnification; (b) high-magnification.

individual tertiary CNC was a well-defined sphere with a rough surface, the size of which was several micrometres. The corresponding high-magnification SEM image (Fig. 3b) reveals that these hematite microspheres are composed of interconnected CNCs as building blocks. That is to say, the hierarchical structure of the tertiary CNCs consists of three levels: the micrometre sized spheres, the secondary CNCs, and the primary nanocrystals. This is the first time that such special hierarchical architecture by CNC self-assembly has been observed to the best of our knowledge. It is a pity that the micrometre size and low yield of tertiary CNCs prevent further study on the internal structure and related properties of such architectures.

Based on the above SEM and TEM results, we proposed that the formation of single-crystal-like spherical hematite CNCs was a simplified self-assembling process, which can be understood as a result of a nucleation–oriented aggregation–recrystallization mechanism from primary nanocrystals under high-temperature solvothermal conditions.[35b] The formation of the spherical hematite CNCs is schematically depicted in Scheme 1. In simple terms, primary hematite nanocrystals firstly nucleate in a supersaturated solution, resulting from the solvent-mediated hydrolysis of Fe^{3+}. The freshly formed nanocrystals are unstable due to their high surface energy, and thus have a great tendency to spontaneously aggregate. During the aggregation process, the adjacent primary nanocrystals align in an orderly way by an oriented-attachment mechanism so that the particles share a planar interface in a common crystallographic orientation.[3,39,40] Therefore, the formed aggregates (*i.e.*, hematite CNCs) present a single-crystal-like characteristic. Meanwhile, the formed aggregates are difficult to grow further due to slow migration once primary nanocrystals within a certain domain are exhausted. As a result, the final aggregates are uniform in size, having a relatively narrow distribution.

In the above mechanism, colloidal primary nanocrystals are generally stabilized by a layer of organic molecules (such as the surfactants or solvents) attached to their surface, and thus the organic–inorganic interface plays a key role in the formation of single-crystal-like spherical hematite CNCs. In order to understand the primary role of the surfactant in the formation process of hematite CNCs, a comparable experiment only without the addition of surfactant PVP was carried out under the same reaction conditions. As shown in Fig. 4a and b, the primary nanocrystals tend to rapidly aggregate in a non-spherical manner, and finally form a bean-like architecture consisting of interconnected hematite nanocrystallites of approximately 35 nm in size. These bean-like hierarchical architectures, which are called bean-like CNCs in our paper, have a wide size distribution from several hundred nanometres to several micrometres in size. The detailed structural information of the bean-like CNCs (Fig. 4c and 4d) from TEM indicates that they are also analogously single-crystal-like, except for more obvious misalignment between primary nanocrystals. The control experiment reveals that the surfactant PVP not only contributed to controlling the size of primary nanocrystals but also contributed to controlling the formation of the spherical geometry. The effects of the surfactant PVP are also shown in Scheme 1.

In the formation of single-crystal-like hematite CNCs, appropriate solvent environment also plays a key role. In our study, we carried out two comparison experiments wherein only a single solvent was used (THF or ethanol) without the addition of surfactant PVP. The product obtained in THF was flower-like hematite, and that in ethanol was bean-like hematite. As shown in Fig. 5a, the flower-like hematite obtained in THF (*i.e.*, flower-like CNCs) is assembled by nanosheets that are composed of numerous primary nanocrystals. The crystallite size of primary nanocrystals calculated from the corresponding XRD pattern (the curve 'a' of Fig. 5d) is about 26 nm, in agreement with the SEM observation. For the bean-like hematite particles obtained in ethanol, they show no obvious hierarchical structures although their shape and structure (Fig. 5b and c) are similar to

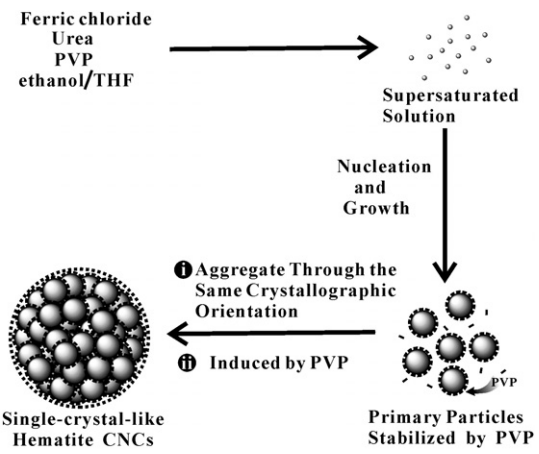

Scheme 1 Schematic representation of the formation of the single-crystal-like spherical hematite CNCs.

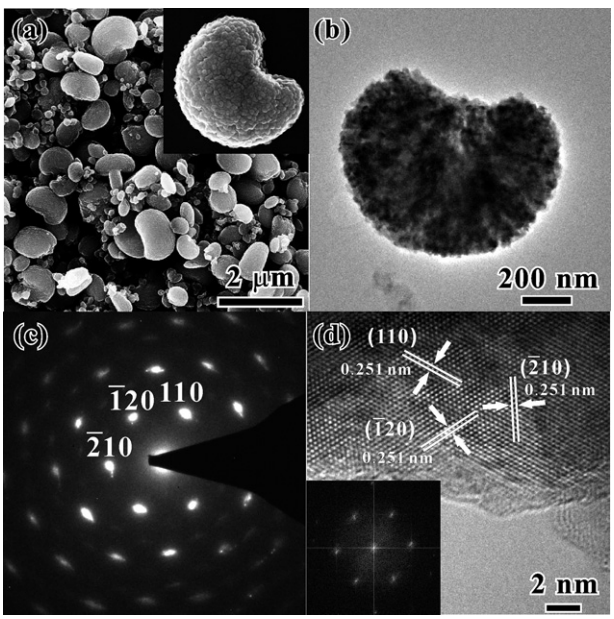

Fig. 4 Bean-like hematite CNCs obtained at the same reaction conditions without the addition of surfactant PVP: (a) low-magnification SEM image (inset: high-magnification SEM image of an individual bean-like hematite CNCs); (b) TEM image and (c) the corresponding SAED pattern of an individual bean-like hematite CNCs; (d) HRTEM image taken from the individual bean-like hematite CNCs (inset: the corresponding FFT pattern).

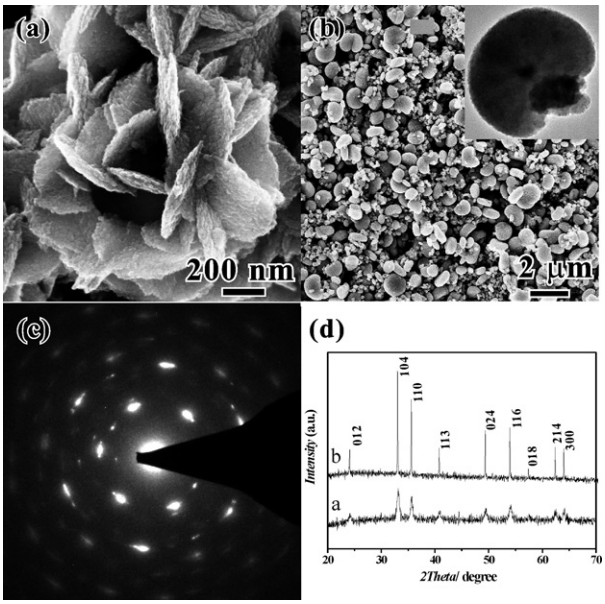

Fig. 5 The hematite nanostructures obtained in single reaction solvent without the addition of surfactant PVP: (a) SEM image of the flower-like hematite CNCs obtained in THF; (b) SEM image of bean-like hematite particles obtained in ethanol (inset: low-magnification TEM image of an individual particle); (c) the corresponding SAED pattern of the bean-like hematite particle shown in the inset of (b); (d) XRD patterns [(a) the flower-like CNCs obtained in THF and (b) the bean-like particles obtained in ethanol].

that of the as-obtained hematite CNCs in the THF–ethanol solvent without the addition of surfactant PVP. This fact is further confirmed by its corresponding XRD pattern (the curve 'b' of Fig. 5d), in which the diffraction peaks of the bean-like hematite particles are not widened. The above results reveal that during the solvent-mediated hydrolysis of Fe^{3+}, THF is responsible for the formation of primary nanocrystals, and ethanol is responsible for the control over the morphology of agglomerated primary nanocrystals. Nevertheless, the final morphology and architecture of formed hematite CNCs depend on the combinatorial role of both the solvents and the surfactant. As persuasive demonstration, more comparison experiments were carried out by changing the ratio of the mixed solvent and the amount of the surfactant PVP (see Fig. S2 in ESI†). The results indicate that the as-prepared hematite is bound to be spherical CNCs on condition that both the mixed solvent of THF–ethanol and the surfactant PVP are used.

The BET surface area of the as-synthesized single-crystal-like spherical hematite CNCs was further investigated by N_2 adsorption–desorption measurements. As shown in Fig. 6, a distinct hysteresis loop is observed in the isotherm of the spherical hematite CNCs. The pore distribution diagram (the inset of Fig. 6) based on the BJH method shows that the spherical hematite CNCs possess small and large mesopore distributions. The small mesopore distribution might originate from the holes between compactly packed primary nanocrystals, and the large mesopore distribution around 30 nm might originate from some vacancies caused by the absence of subunits, as shown in Fig. 1d. For comparison, three other hematite nanostructures obtained in comparison experiments were also measured. Among the four hematite nanostructures, only the spherical CNCs possess porosity, and their surface area is the largest, up to 35.73 $m^2\ g^{-1}$ (Table 1).

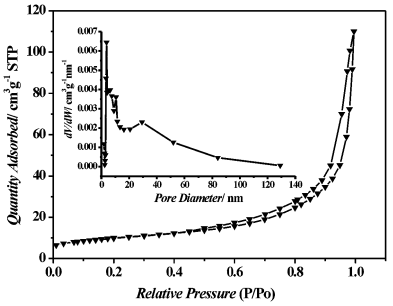

Fig. 6 The nitrogen adsorption–desorption isotherm of the as-obtained spherical hematite CNCs (inset: the pore size distribution curve).

As examples for promising applications, we systematically investigated the properties of the as-synthesized spherical CNCs and other three hematite nanostructures in gas sensing, photocatalysis, and water treatment. As a reference, a commercial hematite powder of 6.0 $m^2\ g^{-1}$ surface area was studied, a typical SEM image of which is shown in Fig. S3 (see ESI†). Fig. 7 shows the gas responsivities of the four hematite nanostructures and commercial hematite powder based sensors as a function of ethanol concentrations. Obviously, the responsivities of the spherical CNCs are much higher than other three hematite nanostructures and commercial powder. When the ethanol concentration is 400 ppm, the responsivity of the spherical CNCs is about 80, which is 12.8 times as great as that of commercial hematite.

The photocatalytic performance of the samples was investigated by monitoring the degradation of RB in the presence of hematite photocatalysts under UV irradiation. Fig. 8 shows real-time degradation curves of RB by using different hematite nanostructures as photocatalysts. The spherical hematite CNCs exhibit superior photoactivity, and total degradation of RB was

Table 1 A summary of the structural features and related performance of the spherical hematite CNCs and other hematite nanostructures synthesized at different solvent environments

Morphology	Solvents	BET surface area/$m^2\ g^{-1}$	Porosity	Responsivity to 400 ppm ethanol	Degradation capacity to RB within 60 min (%)	Removal capacity for Cr^{VI}/mg g^{-1}
Sphere-like CNCs	THF–ethanol (1 : 1), PVP	35.73	Yes	79.7	100	7.0
Flower-like CNCs	THF	26.64	No	55.9	40.6	5.7
Bean-like CNCs	THF–ethanol	12.54	No	21.1	29.5	4.7
Bean-like particles	Ethanol	10.95	No	11.9	23.9	3.8
Commercial hematite	—	6.03	No	6.2	19.7	0.6

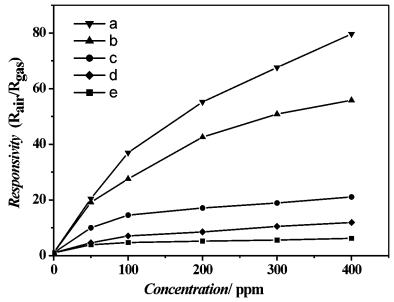

Fig. 7 Responsivities of the as-obtained hematite CNCs to ethanol gases at different concentrations: (a) spherical hematite CNCs, (b) flower-like hematite CNCs obtained in THF, (c) bean-like hematite CNCs obtained only without the addition of surfactant PVP, (d) bean-like hematite particles obtained in ethanol, (e) hematite commercial powder.

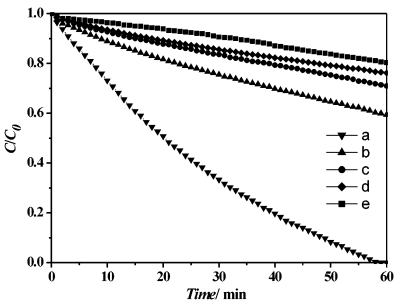

Fig. 8 Degradation rate of RB over different hematite photocatalysts: (a) spherical hematite CNCs, (b) flower-like hematite CNCs obtained in THF, (c) bean-like hematite CNCs obtained only without the addition of surfactant PVP, (d) bean-like hematite particles obtained in ethanol, (e) hematite commercial powder.

completed within 60 min. However, only less than 45% of RB was degraded within the same time for the other hematite nanostructures and commercial powder.

The as-obtained hematite CNCs were extended for potential application in water treatment. Chromium ion (Cr^{VI}) was chosen as the target pollutant, because it is an ideal substrate for evaluation of the water treatment based on the hematite materials. In addition, Cr^{VI} is one of the primary pollutants that require scientists to design methods to reduce it. Fig. 9 shows the maximum adsorption capacities of the spherical hematite CNCs and other hematite nanostructures. Clearly, the spherical hematite CNCs possess a much higher removal capacity for Cr^{VI} (7.0 mg g^{-1}) than the other hematite samples (commercial powder is only 0.6 mg g^{-1}).

Table 1 lists the structural features of all the measured hematite samples and their performances in gas sensing, photocatalysis and removal of metal contaminants. We found that the single-crystal-like spherical hematite CNCs behave as the best among the samples for all the measured properties. In principle, gas sensing, photocatalysis and removal of metal contaminants are related to surface reactions, which greatly depend on the size and surface area of semiconductor nanostructures. Better than the other hematite nanostructures and the commercial hematite powder, the surface area of the as-prepared spherical hematite

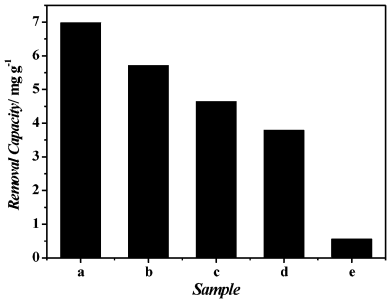

Fig. 9 The maximal removal capacities of Cr^{VI} on as-obtained spherical hematite CNCs: (a) spherical hematite CNCs, (b) flower-like hematite CNCs obtained in THF, (c) bean-like hematite CNCs obtained only without the addition of surfactant PVP, (d) bean-like hematite particles obtained in ethanol, (e) hematite commercial powder.

CNCs is obviously higher. Furthermore, the spherical hematite CNCs possess two types of interior porous structures, which are favorable for adsorption and desorption of the target molecules on the surfaces. Such structural features may primarily be responsible for its excellent performances in these surface-related properties. Taking the photodegradation of RB as an example, it is a kind of surface reaction which typically depends on surface structures of the semiconductor photocatalysts. Besides the surface area, several key surface factors such as the defects, the type of exposed planes, and the porosity of the photocatalysts also influence the RB photodegradation efficiency. Among all the hematite measured, only the spherical CNCs possess the porous structure, and its surface area is also the highest (see Table 1). These features give the spherical hematite CNCs better performance in photodegradation than the other hematite nanostructures.

Compared with the dispersed nanocrystals, our prepared spherical hematite CNCs show other advantages: (1) high surface-to-volume ratios with effective prevention of further aggregation of the nanocrystals, so as to retain high catalytic activities for surface reaction,[18] and (2) easier separation and recycling because of larger diameters of the CNCs. These merits of the spherical hematite CNCs are more helpful for practical applications in some fields than the available dispersed nanocrystals.

Conclusions

In summary, we have successfully demonstrated a facile one-pot synthetic route to prepare a 3D hierarchical hematite nanostructure, *i.e.* spherical CNCs. The as-prepared hematite CNCs are composed of numerous oriented-attached nanocrystals of approximately 20 nm in size, and present a single-crystal-like characteristic. Both the surfactant PVP and the mixed solvent of THF–ethanol play very critical roles in controlling the size of primary nanocrystals and the final morphology of single-crystal-like spherical CNCs. Our results demonstrate that the as-prepared hematite CNCs present excellent properties in the gas sensing, photocatalysis and water treatment, and are expected to be applicable in other fields. Moreover, interesting hierarchical structured hematite microspheres can be further self-assembled from the CNCs through optimization of the initial concentration

of reactants. The implication of the complex hierarchical microstructure growth from the CNCs building blocks may stimulate chemists to explore further other hierarchical self-assemblies starting from experimentally available colloidal nanocrystals.

Acknowledgements

This work was supported financially by the NNSFC (grant nos 20525103, 20531050, 20721001, 20725310, and 20801045) and the 973 Program (grant no. 2007CB815301).

References

1 Y. Sun and Y. Xia, *Science*, 2002, **298**, 2176.
2 Z. A. Peng and X. Peng, *J. Am. Chem. Soc.*, 2002, **124**, 3343.
3 Y. D. Yin and A. P. Alivisatos, *Nature*, 2005, **437**, 664.
4 X. Wang, J. Zhuang, Q. Peng and Y. D. Li, *Nature*, 2005, **437**, 121.
5 (*a*) N. Y. Morgan, C. A. Leatherdate, M. Drndić, M. V. Jarosz, M. A. Kastner and M. Bawendi, *Phys. Rev. B: Condens. Matter*, 2002, **66**, 075339; (*b*) D. V. Talapin, C. T. Black, C. R. Kagan, E. V. Shevchenko, A. Afzali and C. B. Murray, *J. Phys. Chem. C*, 2007, **111**, 13244; (*c*) J. J. Urban, D. V. Talapin, E. V. Shevchenko, C. R. Kagan and C. B. Murray, *Nat. Mater.*, 2007, **6**, 115.
6 (*a*) A. R. Tao, D. P. Ceperley, P. Sinsermsuksakul, A. R. Neureuther and P. D. Yang, *Nano Lett.*, 2008, **8**, 4033; (*b*) C. J. Wang, B. A. Parviz and L. Y. Lin, *Nanotechnology*, 2008, **19**, 295201.
7 (*a*) W. G. Lu, Q. S. Liu, Z. Y. Sun, J. B. He, C. Ezeolu and J. Y. Fang, *J. Am. Chem. Soc.*, 2008, **130**, 6983; (*b*) J. Zhang, A. Kumbhar, J. B. He, N. C. Das, K. K. Yang, J. Q. Wang, H. Wang, K. L. Stokes and A. Y. Fang, *J. Am. Chem. Soc.*, 2008, **130**, 15203.
8 (*a*) J. P. Ge, Y. X. Hu, M. Biasini, W. P. Beyermann and Y. D. Yin, *Angew. Chem., Int. Ed.*, 2007, **46**, 4342; (*b*) J. P. Ge and Y. D. Yin, *J. Mater. Chem.*, 2008, **18**, 5041; (*c*) N. Wang, L. Guo, L. He, X. Cao, C. P. Chen, R. M. Wang and S. H. Yang, *Small*, 2007, **3**, 606.
9 (*a*) K. S. Cho, D. V. Talapin, W. Gaschler and C. B. Murray, *J. Am. Chem. Soc.*, 2005, **127**, 7140; (*b*) W. G. Lu, P. X. Gao, W. B. Jian, Z. L. Wang and J. Y. Fang, *J. Am. Chem. Soc.*, 2004, **126**, 14816.
10 (*a*) E. V. Shevchenko, D. V. Talapin, N. A. Kotov, S. O'Brien and C. B. Murray, *Nature*, 2006, **439**, 55; (*b*) E. V. Shevchenko, M. Ringler, A. Schwemer, D. V. Talapin, T. A. Klar, A. L. Rogach, J. Feldmann and A. P. Alivisatos, *J. Am. Chem. Soc.*, 2008, **130**, 3274; (*c*) E. V. Shevchenko, J. B. Kortright, D. V. Talapin, S. Aloni and A. P. Alivisatos, *Adv. Mater.*, 2007, **19**, 4183.
11 G. M. Whitesides and M. Boncheva, *Proc. Natl. Acad. Sci. U. S. A.*, 2002, **99**, 4769.
12 (*a*) C. A. Mirkin, R. L. Letsinger, R. C. Mucic and J. J. Storhoff, *Nature*, 1996, **382**, 607; (*b*) A. K. Boal, F. Ilhan, J. E. DeRouchey, T. T. Albrecht, T. P. Russell and V. M. Rotello, *Nature*, 2000, **404**, 746.
13 J. Q. Zhuang, H. M. Wu, Y. G. Yang and Y. C. Cao, *Angew. Chem., Int. Ed.*, 2008, **47**, 2208.
14 F. Bai, D. S. Wang, Z. Y. Huo, W. Chen, L. P. Liu, X. Liang, C. Chen, X. Wang, Q. Peng and Y. D. Li, *Angew. Chem., Int. Ed.*, 2007, **46**, 6650.
15 N. C. Bigall, T. Härtling, M. Klose, P. Simon, L. M. Eng and A. Eychmüller, *Nano Lett.*, 2008, **8**, 4588.
16 A. Narayanaswamy, H. F. Xu, N. Pradhan and X. G. Peng, *Angew. Chem., Int. Ed.*, 2006, **45**, 5361.
17 (*a*) T. P. Chou, Q. F. Zhang, G. E. Fryxell and G. Z. Cao, *Adv. Mater.*, 2007, **19**, 2588; (*b*) X. L. Hu, J. M. Gong, L. Z. Zhang and J. C. Yu, *Adv. Mater.*, 2008, **20**, 4845.
18 J. S. Hu, L. L. Ren, Y. G. Guo, H. P. Liang, A. M. Cao, L. J. Wan and C. L. Bai, *Angew. Chem., Int. Ed.*, 2005, **44**, 1269.
19 (*a*) Z. Y. Sun, H. Q. Yuan, Z. M. Liu, B. X. Han and X. R. Zhang, *Adv. Mater.*, 2005, **17**, 2993; (*b*) J. Chen, L. Xu, W. Y. Li and X. L. Gou, *Adv. Mater.*, 2005, **17**, 582.
20 Y. Wang, J. L. Cao, S. R. Wang, X. Z. Guo, J. Zhang, H. J. Xia, S. M. Zhang and S. H. Wu, *J. Phys. Chem. C*, 2008, **112**, 17804.
21 (*a*) X. L. Gou, G. X. Wang, X. Y. Kong, D. Wexler, J. Horvat, J. Yang and J. Park, *Chem.–Eur. J.*, 2008, **14**, 5996; (*b*) G. X. Wang, X. L. Gou, J. Horvat and J. Park, *J. Phys. Chem. C*, 2008, **112**, 15220; (*c*) X. L. Gou, G. X. Wang, J. Park, H. Liu and J. Yang, *Nanotechnology*, 2008, **19**, 125606.
22 M. V. Reddy, T. Yu, C. H. Sow, Z. X. Shen, C. T. Lim, G. V. S. Rao and B. V. R. Chowdari, *Adv. Funct. Mater.*, 2007, **17**, 2792.
23 Z. Z. Zhong, J. Y. Lin, S. P. Teh, J. Teo and F. M. Dautzenberg, *Adv. Funct. Mater.*, 2007, **17**, 1402.
24 Y. H. Zheng, Y. Cheng, Y. S. Wang, F. Bao, L. H. Zhou, X. F. Wei, Y. Y. Zhang and Q. Zheng, *J. Phys. Chem. B*, 2006, **110**, 3093.
25 L. L. Li, Y. Chu, Y. Liu and L. D. Dong, *J. Phys. Chem. C*, 2007, **111**, 2123.
26 (*a*) S. Y. Zeng, K. B. Tang, T. W. Li, Z. H. Liang, D. Wang, Y. K. Wang, Y. X. Qi and W. W. Zhou, *J. Phys. Chem. C*, 2008, **112**, 4836; (*b*) S. W. Cao and Y. Y. Zhu, *J. Phys. Chem. C*, 2008, **112**, 6253.
27 L. S. Zhong, J. S. Hu, H. P. Liang, A. M. Cao, W. G. Song and L. J. Wan, *Adv. Mater.*, 2006, **18**, 2426.
28 S. Y. Zeng, K. B. Tang, T. W. Li, Z. H. Liang, D. Wang, Y. K. Wang and W. W. Zhou, *J. Phys. Chem. C*, 2007, **111**, 10217.
29 Y. Z. Piao, J. Y. Kim, H. B. Na, D. Y. Kim, J. S. Beak, M. K. Ko, J. H. Lee, M. Shokouhimehr and T. Hyeon, *Nat. Mater.*, 2008, **7**, 242.
30 (*a*) X. G. Wen, S. H. Wang, Y. Ding, Z. L. Wang and S. H. Yang, *J. Phys. Chem. B*, 2005, **109**, 215; (*b*) R. M. Wang, Y. F. Chen, Y. Y. Fu, H. Zhang and C. Kisielowski, *J. Phys. Chem. B*, 2005, **109**, 12245.
31 (*a*) C. J. Jia, L. D. Sun, Z. G. Yan, L. P. You, F. Luo, X. D. Han, Y. C. Pang, Z. Zhang and C. H. Yan, *Angew. Chem., Int. Ed.*, 2005, **44**, 4328; (*b*) C. J. Jia, L. D. Sun, Z. G. Yan, Y. C. Pang, L. P. You and C. H. Yan, *J. Phys. Chem. C*, 2007, **111**, 13022.
32 L. Liu, H. Z. Kou, W. L. Mo, H. J. Liu and Y. Q. Wang, *J. Phys. Chem. B*, 2006, **110**, 15218.
33 (*a*) S. B. Wang, Y. L. Min and S. H. Yu, *J. Phys. Chem. C*, 2007, **111**, 3551; (*b*) B. P. Jia and L. Gao, *Cryst. Growth Des.*, 2008, **8**, 1372.
34 X. Liang, X. Wang, J. Zhuang, Y. T. Chen, D. S. Wang and Y. D. Li, *Adv. Funct. Mater.*, 2006, **16**, 1805.
35 (*a*) X. L. Hu, J. C. Yu, J. M. Gong, Q. Li and G. S. Li, *Adv. Mater.*, 2007, **19**, 2324; (*b*) X. L. Hu and J. C. Yu, *Adv. Funct. Mater.*, 2008, **18**, 880.
36 L. P. Zhu, H. M. Xiao, X. M. Liu and S. Y. Fu, *J. Mater. Chem.*, 2006, **16**, 1794.
37 M. H. Cao, T. F. Liu, S. Gao, G. B. Sun, X. L. Wu, C. W. Hu and Z. L. Wang, *Angew. Chem., Int. Ed.*, 2005, **44**, 4197.
38 M. Niedergerge, F. Krumeich, K. Hegetschweiler and R. Nesper, *Chem. Mater.*, 2002, **14**, 78.
39 M. Niedergerge and H. Cölfen, *Phys. Chem. Chem. Phys.*, 2006, **8**, 3271.
40 R. L. Penn and J. F. Banfield, *Science*, 1998, **281**, 969.

